Journal of Catalysis 374 (2019) 101–109

Contents lists available at ScienceDirect

Journal of Catalysis

journal homepage: www.elsevier.com/locate/jcat

PdCu alloy nanoparticles supported on CeO_2 nanorods: Enhanced electrocatalytic activity by synergy of compressive strain, PdO and oxygen vacancy

Zhiwei Guo [a], Xiongwu Kang [b,*], Xusheng Zheng [c], Jie Huang [a,*], Shaowei Chen [b,d]

[a] Department of Chemical Engineering, Shaanxi Key Laboratory of Physico-Inorganic Chemistry, Northwest University, Xi'an, Shanxi 710069, China
[b] New Energy Research Institute, School of Environment and Energy, South China University of Technology, Guangzhou Higher Education Mega Centre, Guangzhou 510006, China
[c] National Synchrotron Radiation Laboratory, University of Science and Technology of China, Hefei 230029, China
[d] Department of Chemistry and Biochemistry, University of California, 1156 High Street, Santa Cruz, CA 95064, United States

ARTICLE INFO

Article history:
Received 18 January 2019
Revised 3 April 2019
Accepted 16 April 2019

Keywords:
PdCu
d-band
Compressive strain
Palladium oxide
Oxygen vacancy
Electrocatalysis

ABSTRACT

Metal oxides have been widely studied as promoter of catalytic performance of metal catalysts through the strong metal-support interactions. However, the mechanism behind it is still debating. Here a series of PdCu nanoparticles with size from 4.9 to 15.4 nm are prepared and loaded on CeO_2 nanorods, which are further characterized by HRTEM, X-ray diffraction (XRD), X-ray photoelectron spectroscopy (XPS) and electrochemical CO stripping. The coupling of PdCu nanoparticles and CeO_2 nanorods induces compressive strain on PdCu nanoparticles, which is strongly dependent on the size of PdCu nanoparticles. The correlation among the compressive strain, down-shift of the *d*-band center, reduced CO binding energy and augmentation of PdO content for PdCu nanoparticles is further discussed in details. Based on comprehensive analyses, it is concluded that the reduced CO oxidation potential on PdCu nanoparticles upon CeO_2 support is from enhanced PdO on PdCu, while the synergy of compressive strain, enhanced PdO and oxygen vacancy remarkably promotes the catalytic performance of PdCu towards electrooxidation of formic acid.

1. Introduction

The rapid consumption of fossil fuel and the tremendous emission of greenhouse gas result in severe environmental problems, thus pushing the researchers to look for alternative renewable and clean energy sources. As a kind of promising clean and portable energy sources for electric vehicles and grid energy storage, direct formic acid fuel cell (DFAFC) and direct methanol fuel cell (DMFC) have stimulated enormous scientific and technological attention in the past decades due to their high power density output, low operating temperatures and zero levels of emissions of noxious pollutants [1–6]. However, the commercialization of such fuels cells is largely limited by the high cost and low catalytic activity of the noble metal catalysts towards the oxidation of the organic fuels [7]. Although Pt exhibited superior electrocatalytic performance towards formic acid oxidation reaction (FAOR) and methanol oxidation reaction (MOR) [8–11], it is readily poisoned by the CO intermediate [12–14]. Compared to Pt catalyst, Pd-based catalysts display improved CO tolerance due to their preferential catalysis toward the dehydrogenation pathway [15–19].

Extensive efforts have been devoted to improve the catalytic performance of these noble metal catalysts. For instance, alloying with an earth-abundant metal (M) could not only reduce the consumption of scarce Pd but also simultaneously modify their electronic structures enhance the catalytic performances [20–22]. For example, alloying with Cu has been demonstrated markedly enhanced CO tolerance and catalytic performance [12,23,24]. Core-shell M@Pd nanostructure has also been recognized as one of such strategies to modulate the lattice strain, electronic structure and catalytic performance of Pd [25,26]. Yang et al. synthesized core-shell structured Cu@Pd catalysts and associated the catalytic performance for formic acid oxidation with the lattice contraction of Pd shell [27].

Metal-support interaction has also demonstrated markedly enhanced catalytic performance of the metal catalysts, but the mechanism behind it remains debating. Some researcher ascribed such enhanced catalytic performance to the strain-induced modification of electronic structures of the catalysts [28,29]. For example,

* Corresponding authors.
E-mail addresses: esxkang@scut.edu.cn (X. Kang), huangjie@nwu.edu.cn (J. Huang).

https://doi.org/10.1016/j.jcat.2019.04.027
0021-9517/

Sun and co-workers reported that the strong interfacial interactions between CuPd particles and $WO_{2.72}$ support, and the enhanced catalytic activity of Pd was ascribed to the tensile strain and reduced electronic density of Pd catalyst [30,15]. Instead, others contribute such enhanced catalytic performance to the surface defects of metal oxide support [3]. Sun et al. ascribed the excellent specific activity and strong anti-poisoning ability during methanol electrooxidation of Pt/CeO_2 to the active oxygen species supplied by CeO_2 with high energy surfaces [31]. Ye and coworkers investigated the size effect of Pt/CeO_2 and contribute the best 1.8 nm Pt nanoparticles on CeO_2 to the balance of the Pt dispersion and oxygen vacancy on CeO_2 support [32]. However, comprehensive study for the metal-oxide support interaction from the two aspects, especially from one research group is barely available in the literature.

Here we report that the PdCu alloy nanoparticles (NPs) of different sizes (6.7 and 14.5 nm) supported on CeO_2 nanorods (NRs) support. Benefiting from the lattice contraction of PdCu alloy induced by CeO_2 (NRs), a downshift of the *d*-band center was observed for PdCu NPs. $PdCu/CeO_2$ catalysts also demonstrate remarkably reduced binding energy of CO and improved catalytic performance towards the formic acid and methanol oxidation, which is 7.5 and 2.4 times that of Pd/C. In addition, the size effect on the metal-support interaction was explored and the smaller PdCu nanoparticles show larger enhancement of electrocatalytic activities than the bigger one.

2. Experimental section

2.1. Chemicals

Palladium (II) acetylacetonate ($Pd(acac)_2$, 98%), copper (II) acetylacetonate ($Cu(acac)_2$, 98%), oleylamine (OAm, 80–90%), borane tert-butylamine complex (BTB, 97%), cerium (III) nitrate hexahydrate ($Ce(NO_3)_3{\cdot}6H_2O$, 99%) and sodium hydroxide (NaOH, 97%) were purchased from Energy Chemical. Nafion (0.5 wt%) and commercial Pd/C were from Alfa Aesar. Hexane (98.5%), ethanol (99%), acetic acid (99.5%) and formic acid (88%) were from Tianjin Damao Chemical Works. Carbon black (Vulcan XC-72) was from Cabot. All chemicals were used as received from commercial suppliers without further treatment. The deionized (DI) water was obtained from a Barnstead Nanopure water system (18.2 MΩ·cm).

2.2. Synthesis of CeO_2 NRs

In a typical synthesis, 0.868 g of $Ce(NO_3)_3{\cdot}6H_2O$ and 9.6 g NaOH were dissolved in 5 and 35 mL of DI water, respectively. Then, the two solutions were mixed in a Teflon bottle and kept stirring for 30 min until the formation of a milky slurry. Finally, the autoclave was transferred into an electric oven and maintained at 100 °C for 24 h. Then the fresh white precipitates were separated by centrifugation, washed with deionized water for several times, followed by drying at 60 °C in air overnight. The obtained yellow powders are CeO_2 NRs with dimension of (10 ± 1.3) nm × (50–200) nm, as evidenced by SEM images in Fig. S1.

2.3. Synthesis of PdCu

Firstly, 5 nm Pd NPs was synthesized through thermal reduction of OAM. Under a nitrogen flow, 61 mg (0.2 mmol) $Pd(acac)_2$ was dissolved in 30 mL OAM and then heated to 60 °C in 10 min. Then 250 mg BTB was solvated in another 3 mL OAm and quickly injected into the above solution. The OAm solution was heated to 90 °C and kept for 60 min. After cooling to room temperature (RT), the OAm solution was added with 30 mL ethanol and the product was separated by centrifugation (8000 rpm, 6 min). The product was then dispersed in hexane. Then, PdCu NPs was synthesized as followed. 52 mg (0.2 mmol) $Cu(acac)_2$ was mixed with 30 mL OAm and magnetically stirred at 80 °C under a gentle N_2 flow for 30 min. Then 21 mg (0.2 mmol) Pd NPs of 5 nm in diameter dispersed in 2 mL hexane was dropped into the solution. The solution was heated to 220 °C and kept for 1 h. When it was cooled to room temperature, and the product was precipitated by adding ethanol and hexane into the OAm solution, separated centrifugation at 9000 rpm for 6 min and further washed with ethanol twice by centrifugation. The final product was denoted as PdCu-1 NPs. The PdCu-2 NPs were synthesized via the same protocol, by adjusting the amount of OAm to 30 mL.

To synthesize PdCu NPs of 10.7 nm, 20 mL OAm in a three-necked flask was first heated to 220 °C under nitrogen atmosphere, to which $Pd(acac)_2$ (0.2 mmol) and $Cu(acac)_2$ (0.2 mmol) in 5 mL OAm was added dropwise in 20 s. The solution was stirred for 1 h and then cooled to RT. The final product was separated by adding ethanol and centrifuging at 9000 rpm for 6 min, washed with ethanol and dispersed in hexane. The derived product was labeled as PdCu-3 NPs. The PdCu-4 and PdCu-5 NPs were synthesized via the same protocol, by adding the Pd and Cu precursor solution in 1 min and 4 min, respectively.

2.3.1. Synthesis of $PdCu/CeO_2$

PdCu alloy nanoparticles were loaded on CeO_2 NRs with a mass ratio of 1:2. In a typical process, 34.4 mg (0.2 mmol) CeO_2 NRs in 3 mL OAm were added into PdCu NPs solution in OAm at 220 °C. After stirring for 30 min, the OAm solution was cooled to RT and the product was further precipitated by adding ethanol and centrifugation and washed multiple times with ethanol to obtain the coupled $PdCu/CeO_2$.

2.4. Characterization

X-ray diffraction (XRD) measurements were carried out on a Bruker D8 diffractometer with Cu Kα radiation (λ = 0.15406 nm). The high-resolution TEM (HRTEM) was obtained on a JEOL JEM-2010. The scanning TEM (STEM) images and electron energy dispersive spectroscopy (EDS) line-scan were obtained on Tecnai G2 F30 of FIE. The X-ray photoelectron spectroscopy (XPS) was acquired on a Phi X-tool instrument.

2.5. Electrochemical measurements

The $PdCu/CeO_2$ and PdCu NPs were loaded onto carbon black (Vulcan XC-72) at a mass ratio of 1:2 and 1:4, respectively, to ensure the same loading of PdCu during catalysis tests, which were treated in acetic acid at 60 °C for 10 h to remove the surfactant and washed with DI water and ethanol sequentially twice at RT [33]. The catalyst ink (1 mg/mL) was prepared by dispersing 1 mg of carbon-supported samples (20 wt% loading) in 1 mL ethanol upon sonication for 2 h. Prior to the catalyst deposition, the glassy carbon electrode (GCE, Φ = 6 mm) was subjected to mechanical polishing with 0.3 μm alumina powders on a polishing microcloth for 20 min and subsequent sonicating in ultra-pure water and sulfuric acid solution (3 M) for 10 min respectively. It was then cleaned under UV-Ozone chamber for 10 min to remove the potential organics contaminants on the electrode surface. The cleaned GCE was coated by 10 μg catalyst ink (1 mg/ml) and dried by air flux in RT, followed by deposition of 5 μL Nafion (0.5 wt%) on top of the nanoparticles and evaporation of solvent in air. The loading of all catalysts was organized in Table S1.

The electrochemical characterizations were carried out on a CHI 650E electrochemical workstation (CH Instruments Inc.), with a

conventional three-electrode system at room temperature (25 °C). The catalyst-coated GCE was used as the working electrode, a SCE (in acidic medium) or Hg/HgO (in alkaline medium) with saturated KCl solution as the reference electrode and a Pt slice as counter electrode. The Pd/C, PdCu, or PdCu/CeO_2 catalysts were first activated by cyclic voltammetric (CV) scans in 0.5 M H_2SO_4 or 1 M KOH aqueous solution at a scan rate of 100 mV s^{-1} and then subject to the characterization of the catalytic activity towards electrooxidation of formic acid in 0.5 M HCOOH in 0.5 M H_2SO_4 solution or methanol oxidation in 1 M methanol in 1 M KOH aqueous solution at a scan rate of 50 mV•s^{-1}.

The CO stripping was investigated in 0.5 M H_2SO_4 solution as described below. First, the 0.5 M H_2SO_4 solution was purged with N_2 for 20 min. Then the chronoamperometric (CA) measurement was initiated at 0.2 V (vs. SCE) after CO bubbling for 5 min. Upon CA measurement finished and CO bubbling stopped, the solution was purged again by N_2 for 20 min, followed by 2 cycles of CV measurement with a scan rate of 5 mV•s^{-1}. The electrochemical surface area (ECSA) was calculated based on CO stripping: ECSA = Q/424W_{Pd}, where Q is the oxidation charge (μC) of CO calculated by dividing the scan rate with the integral area of the CO desorption peak, W_{Pd} represents the total amount of Pd (mg) on the electrode and 420 is the charge (μC•cm^{-2}) required to oxidize a monolayer of CO on the catalyst [34].

3. Results and discussion

The size of PdCu-x (x = 1, 2, 3, 4, 5) NPs was determined to be 4.9 ± 0.4 nm, 6.7 ± 0.5, 10.7 ± 0.8 nm, 14.5 ± 0.7 nm and 15.4 ± 0.5 nm by TEM respectively, as shown in Fig. S2. The interaction of PdCu nanoparticles with CeO_2 was first examined by HRTEM. Take the PdCu-2 nanoparticles as example, shown in Fig. 1. The lattice fringe of 0.227 nm is observed for PdCu-2 without CeO_2 (Fig. 1A and B), which is ascribed to the interplanar distance of face-centered cubic (fcc) PdCu (1 1 1) [35]. Fig. 1D and E showed the TEM and HRTEM images of PdCu/CeO_2-2, where PdCu nanoparticles are well dispersed on CeO_2 NRs and the lattice fringe is determined to be 0.215 nm, much compressed compared to that of pristine PdCu NPs. Fig. 1C and F shows the line scanning for PdCu-2 NPs and PdCu/CeO_2-2. The signal of Pd and Cu overlap very well with each other across the whole nanoparticle for PdCu-2 NPs (Fig. 1C), suggesting the uniform distribution of Pd and Cu over the PdCu alloy nanoparticles. In contrast, upon interaction with CeO_2, Cu element is enriched at the PdCu/CeO_2 interface (Fig. 1F). Similar results were also observed for PdCu-4 and PdCu/CeO_2-4 samples, as shown in Fig. S3. The compressive strain of PdCu nanoparticles might be caused by mismatch of the lattice distance between PdCu and CeO_2 and also the migration of Cu atoms to the PdCu/CeO_2 interface, in agreement with results observed in earlier report [29].

The interaction of PdCu nanoparticles with CeO_2 is further investigated by XRD. The XRD diffraction patterns of PdCu-x and PdCu/CeO_2-x are shown in Fig. S4 respectively. The diffraction pattern of PdCu is between that of fcc Pd and Cu, suggesting the formation of PdCu alloy. The XRD patterns of PdCu-2 and PdCu-4, the diffraction peak from PdCu (1 1 1) are apparently shifted to high diffraction angels with CeO_2 support, suggesting considerably compressed inter-planar distances on PdCu nanoparticles. Based on Bragg's equation,

$$d_{hkl} = \frac{\lambda}{2sin\theta}, \tag{1}$$

$$d_{hkl} = \frac{a_{fcc}}{\sqrt{h^2 + k^2 + l^2}} \tag{2}$$

where λ = 0.154056 nm, θ is diffraction angle in radians, *hkl* is Miller indices and d_{hkl} is the interplanar distance, the interplanar distance of PdCu (1 1 1) can be determined. Take PdCu-2 as example, the interplanar distance is 0.221 and 0.213 nm and lattice parameters (a_{fcc}) 0.3800 and 0.3726 nm for PdCu-2 and PdCu/CeO_2-2, suggesting that compressive strain was introduced to PdCu nanoparticles by CeO_2 support, as observed in TEM analysis. Similar variation of lattice distance and parameters is induced for other PdCu, as shown in Table S2.

$$\frac{\beta cos\theta}{\lambda} = \frac{k}{L_v} + \frac{K_{hkl}}{a_{fcc}}\alpha + \frac{4sin\theta}{\lambda}\varepsilon \tag{3}$$

The crystallite size (L_v), stacking fault (α) and strain effect (ε) of PdCu and PdCu/CeO_2 were estimated based on the Williamson-Hall method [36] *via* Eq. (3), where β is the full-width at half-maximum (FWHM) of the diffraction peak, *k* is the Scherrer constant considering equal to 1, K(1 1 1) = 0.43, K(2 0 0) = 1 and K(2 2 0) = 0.71. With the assistance of the free Fityk software [37], each diffraction peaks of the samples were fitted via Pearson VII function and

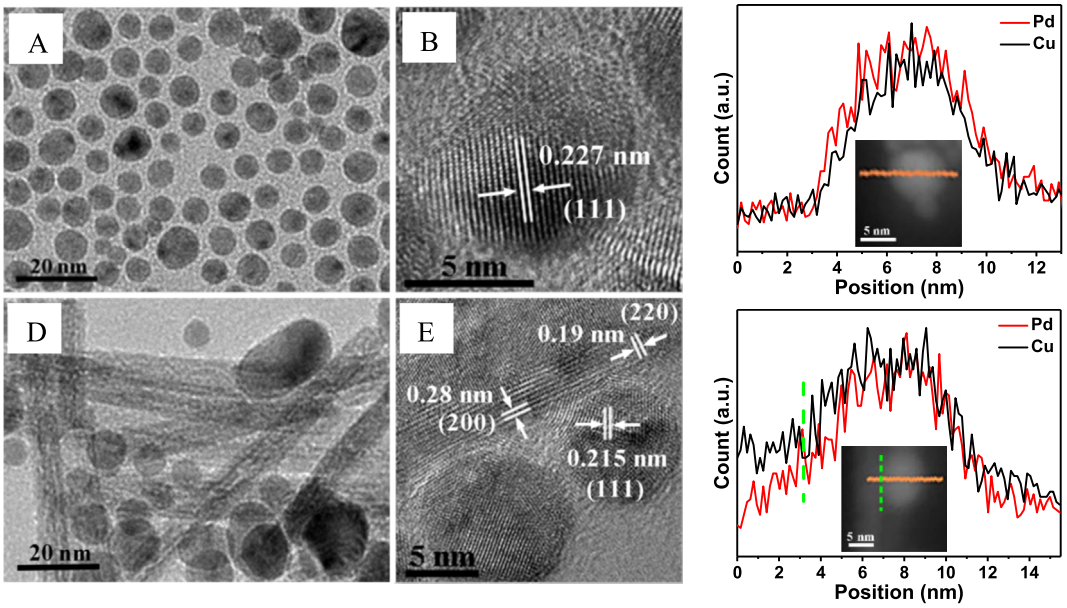

Fig. 1. TEM, HRTEM and STEM-EDS line scan images of PdCu-2 NPs (A, B and C) and PdCu/CeO_2-2 (D, E and F).

Table 1
Parameters evaluated from XRD patterns: interplanar distance (d(1 1 1)/nm), lattice parameter (a_{fcc}/nm), crystallite size (L_v/nm), stacking fault (α/%), and micro-strain (ε/%).

Samples	D (nm)	d (1 1 1)	a_{fcc}	L_v	α	ε
PdCu-2	6.7	0.221	0.3800	7.63	4.23	1.33
PdCu/CeO_2-2		0.213	0.3726	8.03	4.04	1.72
PdCu-4	14.5	0.221	0.3792	14.63	3.32	0.39
PdCu/CeO_2-4		0.214	0.3750	14.96	3.18	0.66

depicted in Fig. S4. The calculated lattice parameter of (a_{fcc}), d (1 1 1), L_v, α and ε are listed in Table 1. It is observed that the L_v and d(1 1 1) value of PdCu and PdCu/CeO_2 are very close to the particle diameters and interplanar distance determined by HRTEM. In addition, larger stacking fault (α) and micro-strain (ε) are observed for smaller PdCu nanoparticles than the larger one, suggesting that the smaller PdCu nanoparticles possess more surface defects [38]. After coupling with CeO_2, the stacking fault (α) is reduced but the micro-strain (ε) is slightly increased for PdCu due to the reconstruction of the PdCu nanoparticles surface.

The lattice strain (s) of the PdCu alloy is determined by using the following Eq. (4) [39]:

$$s = \frac{a_2 - a_1}{a_1} \times 100 \quad (4)$$

where a_1 and a_2 are the lattice parameters of the PdCu alloy in PdCu NPs and PdCu/CeO_2, respectively [25]. As shown in Fig. 2B, the compressive strain of PdCu NPs induced by CeO_2 NRs is strongly dependent on the size of PdCu nanoparticles, which decreased 1.89–0.87% when the diameter of PdCu alloy nanoparticles increased from 4.9 to 15.4 nm, suggesting that larger strain is induced on smaller nanoparticles [28].

By using the analysis of XRD line broadening and the single-line method, the variation of the microstrain (ε′) of CeO_2 (1 1 1), (2 0 0) and (2 2 0) crystal planes upon loading of PdCu is estimated [40,41], which is strongly related with defects such as oxygen vacancies, kinks, steps and dislocation etc., and through which PdCu and CeO_2 are coupled. PdCu/CeO_2-2 and PdCu/CeO_2-4 are analyzed as examples and shown in Table 2. The micro-strain of CeO_2 (2 2 0) increased from 1.53 to 1.89 for PdCu/CeO_2-2 and to 1.79 for PdCu/CeO_2-4, while no apparent variation is observed for CeO_2 (2 0 0) and (1 1 1) facets, suggesting that more defects are induced on CeO_2 (2 0 0) facets by loading of PdCu nanoparticles, through which PdCu NPs and CeO_2 are coupled. In addition, it should be noted that PdCu-2 induces more change of micro-strain on CeO_2 (2 2 0) facets than PdCu-4, possibly due to smaller size and more defects of PdCu-2.

The chemical state of Pd and the atomic percentage of Pd^{2+} of PdCu-x with and without CeO_2 support are strongly related with the performance of the metal catalyst [25,42]. Figs. 3 and S6 show the high resolution XPS spectra of Pd 3d for PdCu-X and PdCu/CeO_2-X, which are deconvoluted into two pairs of doublets. The peaks at 335.0 and 340.35 eV are assigned to the binding energies of Pd(0) 3d5/2 and 3d3/2, and these at 335.6 and 341.0 eV are attributed to Pd(II) 3d5/2 and 3d3/2, respectively [43]. Similarly, the high resolution XPS spectra of Cu 2p in PdCu and PdCu/CeO_2 are equally deconvoluted into two pairs of doublets (Fig. 3B). The peaks at 932.4 and 952.2 eV are assigned to the binding energies of Cu(0) 2p3/2 and 2p1/2, and the binding energy for Cu(II) 2p3/2 and 2p1/2 are identified at 933.6 and 953.6 eV, respectively [30]. Fig. S6A shows the high resolution XPS spectra of Ce 3d in CeO_2 and PdCu/CeO_2. The deconvoluted peaks at 881.6, 887.74 and 897.35 eV are assigned to Ce^{4+}, while that at 884.17 eV is assigned to the Ce^{3+} [3]. Based on the XPS analysis, the atomic ratio of Pd(II) in all Pd content and Ce^{3+} in all Ce content is determined and listed in Table S3.

As shown in Table S3, the Pd^{2+} fraction in PdCu is increased by 15% upon coupling with CeO_2 support, in agreement with earlier report. However, no apparent size effect was observed on the change of PdO content induced by CeO_2 support. It should be noted that the Pd-CeO_2 interactions induce a significant change on the oxidation state of Pd [44] and the rich Pd-PdO interface may promote the electrooxidation of formic acid through the dehydrogenation pathway [45]. Meanwhile, the surface Ce^{3+} (oxygen vacancy) fractions is increased from 14.6% for pristine CeO_2 to 21.2% for PdCu/CeO_2-2, 19.6% for PdCu/CeO_2-3 and 15.8% for PdCu/CeO_2-4 (Table S3), respectively. It can be seen that larger enhancement of oxygen vacancy on CeO_2 was observed for smaller PdCu nanoparticles, indicating a dependence on the size of PdCu nanoparticles. This is also in agreement with the micro-strain analysis, where more micro-strain on CeO_2 NRs was induced by PdCu nanoparticles. These oxygen vacancies may promote the dispersion of nanoparticles on the substrate and further the catalytic activity [3].

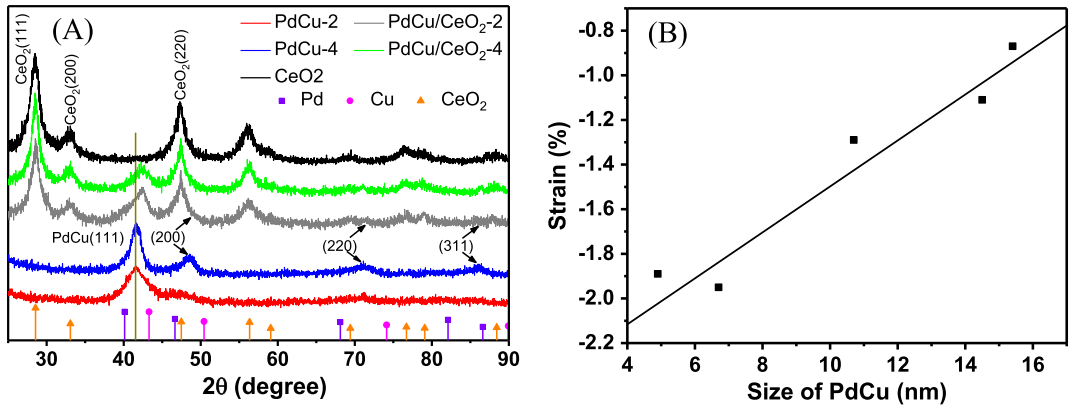

Fig. 2. XRD patterns of (A) PdCu-2 and PdCu-4 with/without CeO_2 support; (B) dependence of compressive strain induced by support of CeO_2 NRs on the size of PdCu nanoparticles.

Table 2
Lattice micro-strain (ε')[a] of different crystal planes of CeO_2 NRs and PdCu/CeO_2-2 and PdCu/CeO_2-4.

Samples	(1 1 1)	ε' [%] (2 0 0)	(2 2 0)
CeO_2 NRs	2.51	2.49	**1.53**
PdCu/CeO_2-2	2.50	2.44	**1.89**
PdCu/CeO_2-4	2.50	2.43	**1.79**

[a] Determined from the analysis of XRD line broadening by the single-line method using a pseudo-Voigt profile function [40,41].

Fig. 3C and D displays the representative valence band spectra of PdCu and PdCu/CeO_2. The *d*-band width of PdCu-2 and PdCu-4 is 4.80 and 4.85 eV respectively, which is quite the same to each other. Upon coupling with CeO_2, the *d*-band width is increased to 6.1 eV and 5.70 eV for PdCu-2 and PdCu-4 respectively, with larger variation observed for smaller nanoparticles. Such broadening of the *d*-band is attributed to the compressive strain of the PdCu lattice, which increases the electronic states overlap between the metal atoms [27,39]. To keep the d-occupancy constant, a downward shift of the *d*-band center occurs, as evidenced by the positive shift of the binding energy of the peak in the valence band spectra in Fig. 3C and D [46–48]. It is observed that the *d*-band center is shifted from −2.2 to −3.9 eV for PdCu-2 and −1.5 to −2.8 eV for PdCu-4 upon coupling with CeO_2. More compressive strain induced on PdCu-2 results in more down-shift of the *d*-band center. Such lowered *d*-band center of PdCu could weaken the chemisorption energy of some reaction intermediates, such as H_2 and CO, on the Pd catalysts surface, thus alleviating the poisoning effect and promoting the electrocatalytic activity and stability [49,50].

To evaluate the CO adsorption energy, the CO-stripping voltammograms of the PdCu and PdCu/CeO_2 of different sizes are measured in 0.5 M H_2SO_4 solution at a scan rate of 5 mV·s^{-1}, as shown in Fig. S7. For PdCu/C and PdCu/CeO_2 catalysts, a typical CO oxidation peaks in the range of 0.6–0.8 V are observed in the first forward CV scan, and then disappear in the subsequent CV scans, accompanied with the emergence of H deposition features in the potential window of −0.25 to 0.0 V, due to the complete removal of the adsorbed CO on the surface of the catalysts in the first CV scan. The CO oxidation peak potential of all PdCu nanoparticles with and without CeO_2 support was derived from CO-stripping voltammetry and listed in Table S4, and the ECSA of these catalysts are calculated and listed in Table S5. It is observed that PdCu/CeO_2 display slightly large ECSA than PdCu, probably due to the enhanced dispersity of PdCu NPs on CeO_2 support.

As shown in Table S4, the peak potential of CO oxidation of PdCu is lowered by 50 mV upon CeO_2 support, suggesting weakened adsorption of CO on PdCu/CeO_2. Surprisingly, reduction of CO oxidation potential keeps constant for all the five PdCu nanoparticle and no size dependence was observed at all. Usually

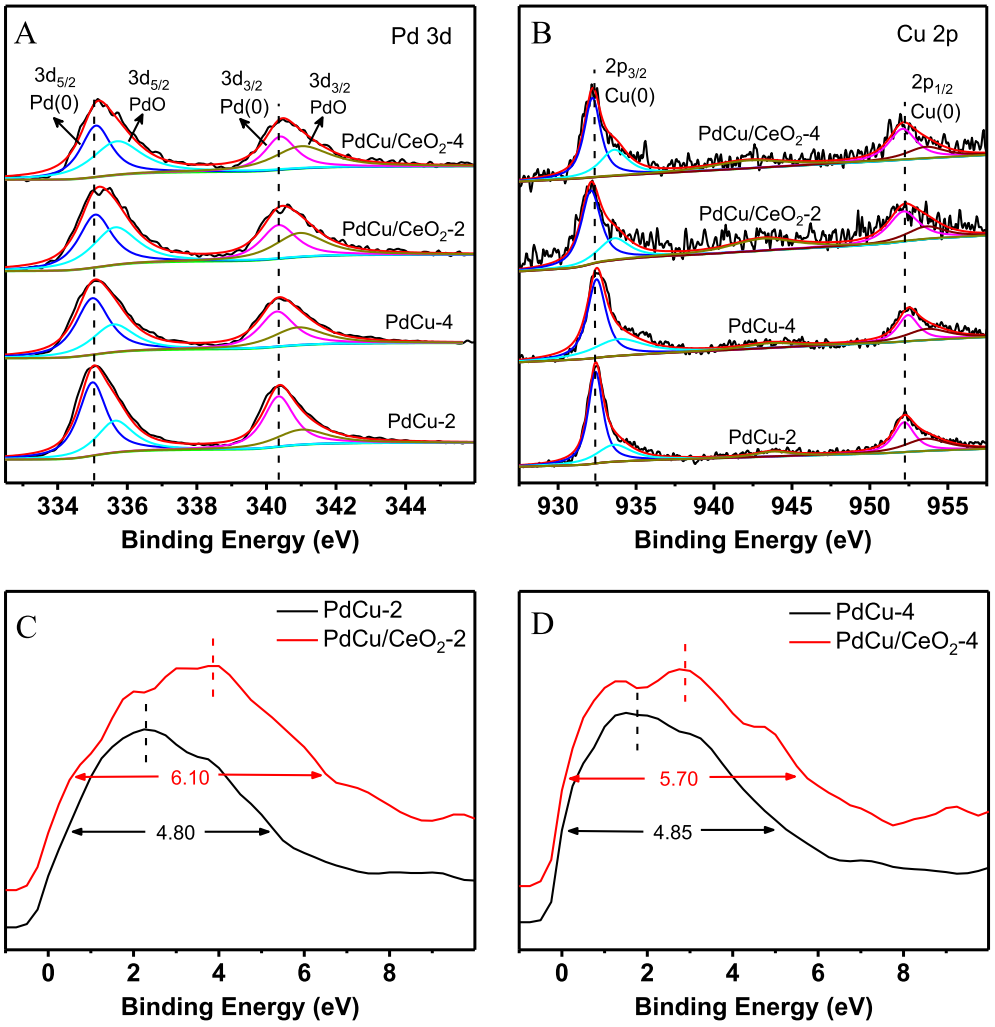

Fig. 3. The high resolution XPS spectra of (A) Pd 3d and (B) Cu 2p for PdCu-2, PdCu/CeO_2-2, PdCu-4 and PdCu/CeO_2-4; Valence band spectra for (C) PdCu-2 and PdCu/CeO_2-2 and (D) PdCu-4 and PdCu/CeO_2-4.

the reduced adsorption energy of CO on Pd is attributed to the down-shift of the *d*-band center of PdCu as demonstrated in Fig. 3 [47,49]. However, although the down-shift of the *d*-band center of PdCu-2 and PdCu-4 induced by CeO_2 support are very different with each other, the reduction of the CO adsorption energy on PdCu-2 and PdCu-4 induced by CeO_2 NRs is the same, as highlighted in Fig. 4, suggesting that such weakened CO adsorption on PdCu/CeO_2 might not be from the down-shift of the *d*-band center. By using density functional theory and Monte Carlo method, J. M. Hensen lately revealed that higher oxidation degree of Pd clusters could reduce CO binding energy and promote the CO oxidation with an oxygen atom from CeO_2 [51]. According to XPS analysis, both PdCu demonstrate the same augmentation of PdO with CeO_2 NRs support, in excellent agreement with the reduction of CO binding energy of PdCu. This suggests that such lowered CO binding energy on PdCu upon coupling with CeO_2 support is from the enhanced oxidation degree of PdCu by CeO_2 support, instead of the lowered *d*-band center induced by the compressive strain.

3.1. Electrooxidation of formic acid

The electrocatalytic performance of all PdCu and PdCu/CeO_2 of different sizes towards FAOR were evaluated in 0.5 M H_2SO_4 + 0.5 M HCOOH aqueous solution, as shown in Fig. S8A and B, from which the specific activity is derived and listed in Table 3.[52]. Fig. S8C and D showed the CV scans of PdCu/C, PdCu/CeO_2/C and Pd/C catalysts in 0.5 M H_2SO_4 solution. The anodic current between −0.25 and 0.1 V is ascribed to the desorption of hydrogen and sulfate anion on the PdCu surfaces [46,53] and the cathodic peaks around 0.4 V are ascribed to the reduction of PdCu. Apparently, the surface area of PdCu is largely enhanced upon coupling with CeO_2 support, suggesting the much-enhanced oxygen species on PdCu surfaces (see Scheme 1).

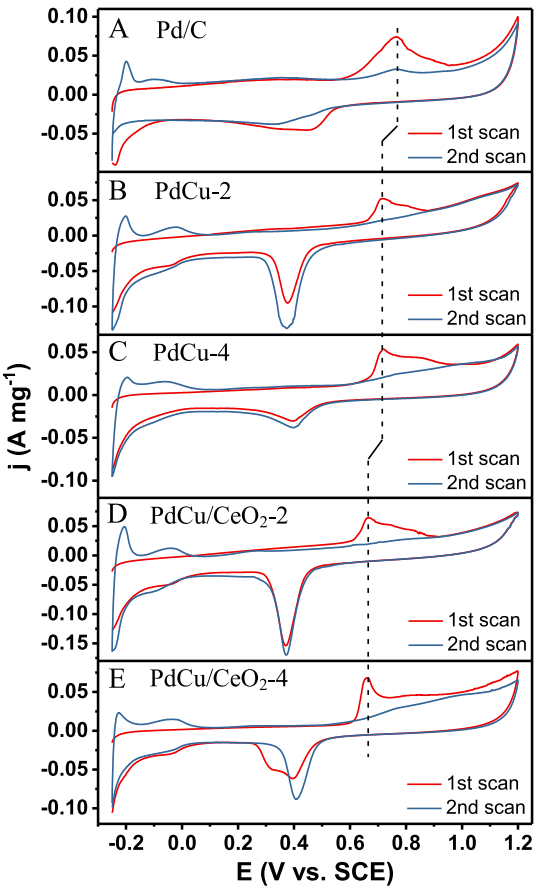

Fig. 4. Cyclic voltammograms of CO-stripping on the commercial Pd/C catalyst (A), PdCu/C-2 (6.7 nm) (B), PdCu/C-4 (14.5 nm) (C), PdCu/CeO_2-2 (D) and PdCu/CeO_2-4 (E) in 0.5 M H_2SO_4 at a scan rate of 50 mV·s^{-1}.

The dependence of the specific activity of PdCu nanoparticles on the size of PdCu nanoparticles with and without CeO_2 are shown in Fig. 5(A), both of which shows a volcano-shape dependence on the size of PdCu alloy nanoparticles. For PdCu nanoparticles, maximum specific activity was achieved at the size of 14.5 nm while that with CeO_2 support reached maximum at 6.7 nm. The enhancement of SA of PdCu nanoparticles by CeO_2 support equally shows apparent size effect (green line), which decreases with the size of PdCu nanoparticles and reach minimum at the size of 14.5 nm. Since the compressive strain of PdCu nanoparticles induced by CeO_2 support decreases linearly with the size of PdCu nanoparticles, thus, it is concluded that the enhancement of specific activity of PdCu nanoparticles strongly dependent on the compressive strain induced by the CeO_2 support, which shows an inverse volcano-shape dependence on the change of the compressive strain of PdCu nanoparticles induced by CeO_2 support.

Among all these catalysts, PdCu/CeO_2-2 demonstrates the highest specific activity (4.7 mA·cm^{-2}) and mass activity (1.72 A·mg_{Pd}^{-1}), which is **9.4** and **7.5 times** that of Pd/C (0.23 A·mg_{Pd}^{-1}). Although PdCu nanoparticles share the same CO adsorption energy, the specific activity is different from each other. This suggests that the difference of catalytic activity of PdCu is not only governed by the CO poisoning effect, but other factors, such as the surface defects and exposed facets of PdCu as reflected by the analysis of XRD and the desorption features of hydrogen and sulfate anions on PdCu (Fig S8C and D) may play roles [46].

According to the analysis above, the enhanced specific activity of PdCu by CeO_2 support is partially attributed to the augmentation of PdO content and the Pd-PdO interface, as demonstrated by XPS analysis, which is active in pulling the hydrogen from the reaction intermediates due to the higher affinity to H^* and promote the electrooxidation of formic acid through the dehydrogenation pathway, bypassing the dehydration pathway and CO poisoning [18,45]. In addition, the weakened adsorption of CO induced by the enhanced PdO content through CeO_2 support may also promote the catalytic performance.[46] In addition, XPS analysis demonstrates that the oxygen vacancies in CeO_2 have increased from 14.6% for pristine CeO_2 to 15.8% upon loading of PdCu, which increases up to 21.2% with the size of PdCu nanoparticles (Table S3). Thus, it is highly possible that such increased oxygen vacancies [3,31] in PdCu/CeO_2 promote the formic acid oxidation. The micro-strain and stacking fault of PdCu-2 and PdCu-4 is thoroughly analyzed by XRD, which is a direct reflection of surface defects such as kinks, steps and dislocation etc. [40,41], through which PdCu nanoparticles coupled with CeO_2. Smaller PdCu nanoparticles demonstrate larger micro-strain and stacking fault, and induce stronger coupling with CeO_2 and more oxygen vacancies on CeO_2 NRs, in agreement with the variation trend of the catalytic activity (Fig. 5B). Thus, we conclude here that the synergy of both the PdO content and oxygen vacancy in CeO_2 NRs promote the catalytic activity of PdCu/CeO_2.

The catalytic activity of PdCu-2 and PdCu-4 towards methanol oxidation is examined and shown in Table S5 and Fig. S9. The specific activity of PdCu-4 and PdCu/CeO_2-4 towards methanol oxidation is almost identical to each other, although PdO content, CO adsorption energy and *d*-band center are apparently changed by CeO_2 NRs, and the oxygen vacancy on CeO_2 NRs changes slightly. This suggests that the factors of PdO, CO adsorption energy and *d*-band center do not contribute to the catalytic activity of PdCu-4 towards methanol. However, PdCu/CeO_2-2 shows apparent enhancement of catalytic activity as compared to PdCu-2, consistent with the more augmentation of oxygen vacancy on CeO_2

Table 3
The ECSA and specific activity (SA) of PdCu electrocatalysts towards FAOR in 0.5 M H_2SO_4 + 0.5 M HCOOH derived from Fig. S8.

Samples	D (nm)	ECSA-PdCu ($m^2\ g^{-1}$)	ECSA-PdCu/CeO_2 ($m^2\ g^{-1}$)	SA-PdCu (mA cm^{-2})	SA-PdCu/CeO_2 (mA cm^{-2})	ΔSA (mA cm^{-2})
PdCu-1	4.9	31.2	36.5	1.7	4.2	2.5
PdCu-2	6.7	29.9	36.6	2.4	4.7	2.3
PdCu-3	10.7	26.6	32.1	2.6	4.4	1.8
PdCu-4	14.5	25.1	31.9	3.5	4.2	0.7
PdCu-5	15.4	25.0	29.7	3.0	3.9	0.9

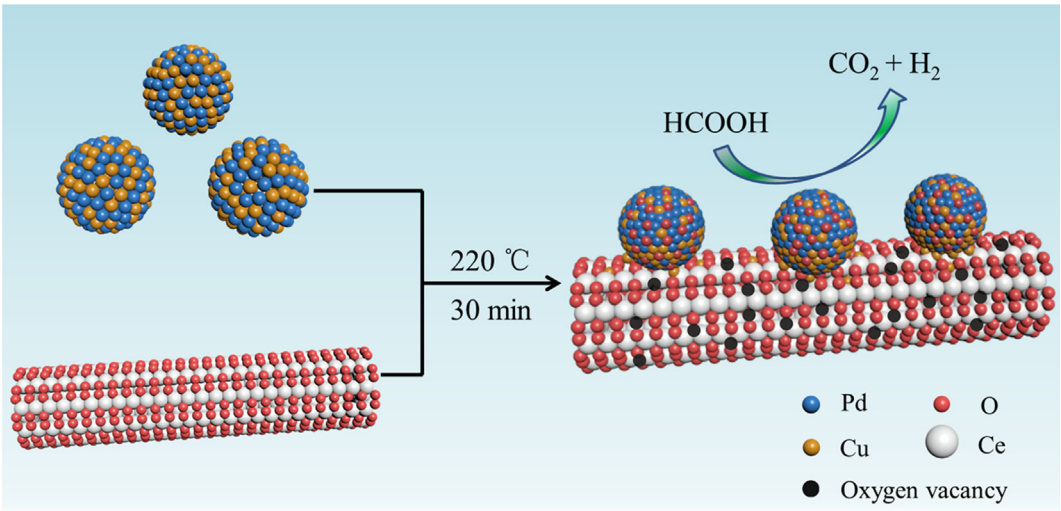

Scheme 1. Schematic illustration of the synthesis of PdCu/CeO_2 and the enhanced catalytic activity by the PdO and oxygen vacancy induced by the oxide support.

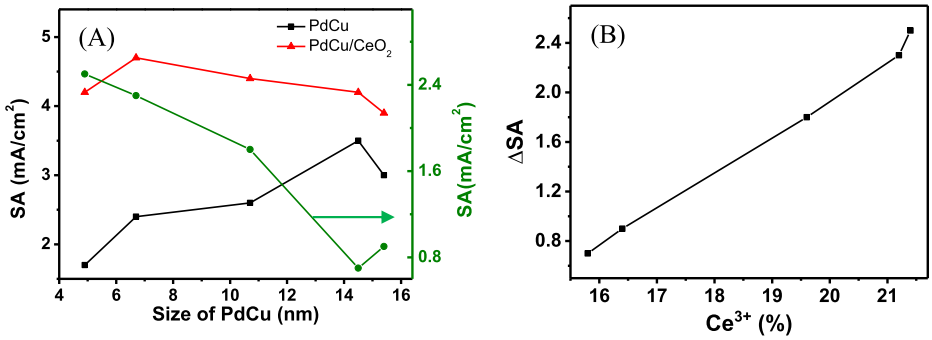

Fig. 5. Dependence of specific activity (SA) (left axis) of PdCu and PdCu-CeO_2 nanoparticles and the enhancement of SA (right axis) of PdCu nanoparticles upon CeO_2 support on the size of PdCu nanoparticles (A) and the concentration of oxygen vacancy (B).

NRs. This might indicate the augmentation of the oxygen vacancy is promoting the electrochemical oxidation of PdCu-2 towards electrochemical oxidation of methanol [54,55].

The cycling stability of PdCu/CeO_2, PdCu and Pd/C for FAOR in the potential window of −0.2 and 0.8 V (vs. SCE) at a scan rate of 50 mV·s^{-1} is carried out and shown in Fig. 6. After 500 sweeping cycles, Pd/C loses 75.2% of its initial mass activity, and the PdCu-2 and PdCu-4 lose 79% and 78.2% of their initial activity, respectively. However, the mass activity of PdCu/CeO_2-2 and PdCu/CeO_2-4 decay by 48.3% and 54.1% after 500 sweeping cycles, respectively, suggesting much improved cycling stability of PdCu nanoparticles by CeO_2 NRs [56]. The CA measurements of PdCu/CeO_2, PdCu and Pd/C catalysts were recorded at 0.2 V (versus SCE) for 1000 s in 0.5 M H_2SO_4 + 0.5 M HCOOH aqueous solution, as displayed in Figs. S10 and 11. The slower decay rate of the PdCu/CeO_2 suggests improved durability than PdCu and the commercial Pd/C catalyst. CV scans of PdCu/CeO_2 before and after CA measurements are almost identical to each other, indicating that the catalyst itself is stable and the current decay in CA measurement was mainly resulted from the poisoning intermediates during the formic acid oxidation, instead of the destruction of the catalyst themselves [36].

4. Conclusions

In this study, a series of PdCu alloy NPs with diameter of 4.9, 6.7, 10.7, 14.5 and15.4 nm was prepared and the interfacial interaction of PdCu alloy NPs with CeO_2 NRs support was examined by TEM, XRD, XPS and CO stripping. It is observed that CeO_2 NRs induce apparent compressive strain on PdCu alloy nanoparticles through the facets of CeO_2 (2 2 0) and PdCu (1 1 1), which further broadened the *d*-band and lowered their *d*-band center of PdCu nanoparticles. Such compressive strain induced by CeO_2 support shows

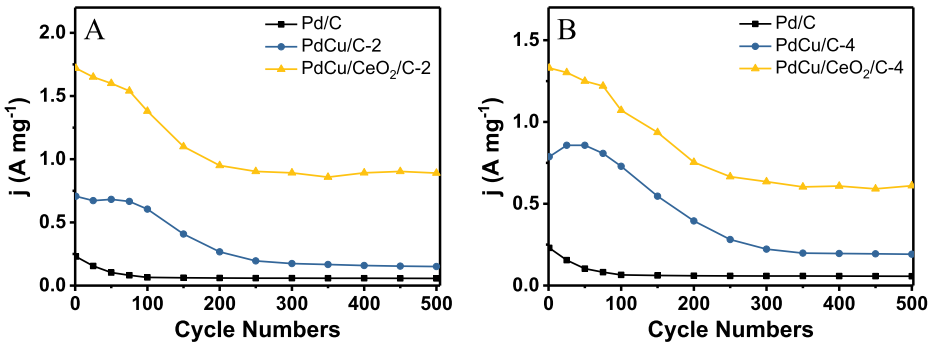

Fig. 6. (A, B) Cycling stability of Pd-based electrocatalysts in 500 cycles between −0.2 and 0.8 V (vs. SCE) in 0.5 M H_2SO_4 + 0.5 M HCOOH aqueous solution at a scan rate of 50 mV·s^{-1}.

apparent size effect, which decreases with the size of PdCu nanoparticles. The reduced CO adsorption energy was ascribed to the augmentation of PdO due to the CeO_2 support. These PdCu and CeO_2 supported catalysts display much enhanced catalytic activity toward FAOR and MOR, which is ascribed to the synergy of compressive strain, augmentation of the surface Pd oxide and the oxygen vacancies on CeO_2 NRs. This work exclusively unraveled the mechanism of the enhanced catalytic activity of metal catalyst by CeO_2 nanorods support, which may shed light on rational design of high-performance anode catalyst of fuel cell.

Acknowledgements

This work was supported by the National Natural Science Foundation of China (No. 51602106), The Natural Science Basic Research of Shaanxi Province (No. 2018JM2061) and Guangdong Innovative and Entrepreneurial Research Team Program (No. 2016ZT06N569).

Conflict of interest

The authors declare no conflict of interest.

Appendix A. Supplementary material

SEM of CeO_2 and TEM histograms of PdCu nanoparticles; HRTEM, XPS and elemental mapping for PdCu-4 and PdCu/CeO_2-4; XRD deconvolution of PdCu, PdCu/CeO_2 and CeO_2; electrochemical performance test of PdCu and PdCu/CeO_2 towards formic acid and methanol oxidation. Supplementary data to this article can be found online at https://doi.org/10.1016/j.jcat.2019.04.027.

References

[1] W. Zhang, P. Sherrell, A.I. Minett, J.M. Razal, J. Chen, Carbon nanotube architectures as catalyst supports for proton exchange membrane fuel cells, Energy Environ. Sci. 3 (2010) 1286–1293.
[2] T. Matsumoto, T. Komatsu, K. Arai, T. Yamazaki, M. Kijima, H. Shimizu, Y. Takasawa, J. Nakamura, Reduction of Pt usage in fuel cell electrocatalysts with carbon nanotube electrodes, Chem. Commun. (Camb) 840–841 (2004).
[3] J. Wang, B. Li, T. Yersak, D. Yang, Q. Xiao, J. Zhang, C. Zhang, Recent advances in Pt-based octahedral nanocrystals as high performance fuel cell catalysts, J. Mater. Chem. A 4 (2016) 11559–11581.
[4] J.M. Sieben, M.M.E. Duarte, C.E. Mayer, Electro-oxidation of methanol on Pt-Ru nanostructured catalysts electrodeposited onto electroactivated carbon fiber materials, ChemCatChem 2 (2010) 182–189.
[5] S. Jones, K. Tedsree, M. Sawangphruk, J.S. Foord, J. Fisher, D. Thompsett, S.C.E. Tsang, Promotion of direct methanol electro-oxidation by Ru terraces on pt by using a reversed spillover mechanism, ChemCatChem 2 (2010) 1089–1095.
[6] C. Alegre, M.E. Galvez, R. Moliner, V. Baglio, A. Stassi, A.S. Arico, M.J. Lazaro, Platinum ruthenium catalysts supported on carbon xerogel for methanol electro-oxidation: influence of the catalyst synthesis method, ChemCatChem 5 (2013) 3770–3780.
[7] C. Rice, S. Ha, R.I. Masel, A. Wieckowski, Catalysts for direct formic acid fuel cells, J. Power Sources 115 (2003) 229–235.
[8] Y. Lu, W. Chen, One-pot synthesis of heterostructured Pt-Ru nanocrystals for catalytic formic acid oxidation, Chem. Commun. (Camb) 47 (2011) 2541–2543.
[9] Z. Qi, C. Xiao, C. Liu, T.W. Goh, L. Zhou, R. Maligal-Ganesh, Y. Pei, X. Li, L.A. Curtiss, W. Huang, Sub-4 nm PtZn intermetallic nanoparticles for enhanced mass and specific activities in catalytic electrooxidation reaction, J. Am. Chem. Soc. 139 (2017) 4762–4768.
[10] B.W. Zhang, T. Sheng, Y.X. Wang, X.M. Qu, J.M. Zhang, Z.C. Zhang, H.G. Liao, F.C. Zhu, S.X. Dou, Y.X. Jiang, S.G. Sun, Platinum-cobalt bimetallic nanoparticles with Pt skin for electro-oxidation of ethanol, ACS Catal. 7 (2017) 892–895.
[11] S. Guo, S. Zhang, X. Sun, S. Sun, Synthesis of ultrathin FePtPd nanowires and their use as catalysts for methanol oxidation reaction, J. Am. Chem. Soc. 133 (2011) 15354–15357.
[12] S.H. Han, H.M. Liu, P. Chen, J.X. Jiang, Y. Chen, Porous trimetallic PtRhCu cubic nanoboxes for ethanol electrooxidation, Adv. Energy Mater. 8 (2018) 1801326-.
[13] W. Chen, S. Chen, Iridium-platinum alloy nanoparticles: composition-dependent electrocatalytic activity for formic acid oxidation, J Mater. Chem. 21 (2011) 9169.
[14] M. Osawa, K. Komatsu, G. Samjeske, T. Uchida, T. Ikeshoji, A. Cuesta, C. Gutierrez, The role of bridge-bonded adsorbed formate in the electrocatalytic oxidation of formic acid on platinum, Angew. Chem. Int. Ed. Engl. 50 (2011) 1159–1163.
[15] Z. Xi, D.P. Erdosy, A. Mendoza-Garcia, P.N. Duchesne, J. Li, M. Muzzio, Q. Li, P. Zhang, S. Sun, Pd nanoparticles coupled to WO2.72 nanorods for enhanced electrochemical oxidation of formic acid, Nano Lett. 17 (2017) 2727–2731.
[16] X. Huang, S. Tang, X. Mu, Y. Dai, G. Chen, Z. Zhou, F. Ruan, Z. Yang, N. Zheng, Freestanding palladium nanosheets with plasmonic and catalytic properties, Nat. Nanotechnol. 6 (2010) 28.
[17] J. Chang, L. Feng, C. Liu, W. Xing, X. Hu, An effective Pd-Ni(2)P/C anode catalyst for direct formic acid fuel cells, Angew. Chem. Int. Ed. Engl. 53 (2014) 122–126.
[18] F.M. Li, Y.Q. Kang, R.L. Peng, S.N. Li, B.Y. Xia, Z.H. Liu, Y. Chen, Sandwich-structured Au@polyallylamine@Pd nanostructures: tuning the electronic properties of the Pd shell for electrocatalysis, J. Mater. Chem. A 4 (2016) 12020–12024.
[19] J. Ge, P. Wei, G. Wu, Y. Liu, T. Yuan, Z. Li, Y. Qu, Y. Wu, H. Li, Z. Zhuang, X. Hong, Y. Li, Ultrathin palladium nanomesh for electrocatalysis, Angew. Chem. Int. Ed. Engl. 57 (2018) 3435–3438.
[20] Y. Lu, W. Chen, Nanoneedle-covered Pd–Ag nanotubes: high electrocatalytic activity for formic acid oxidation, J. Phys. Chem. C 114 (2010) 21190–21200.
[21] X. Kang, K. Miao, Z. Guo, J. Zou, Z. Shi, Z. Lin, J. Huang, S. Chen, PdRu alloy nanoparticles of solid solution in atomic scale: size effects on electronic structure and catalytic activity towards electrooxidation of formic acid and methanol, J. Catal. 364 (2018) 183–191.
[22] L. Huang, J. Yang, M. Wu, Z. Shi, Z. Lin, X. Kang, S. Chen, PdAg@Pd core-shell nanotubes: superior catalytic performance towards electrochemical oxidation of formic acid and methanol, J. Power Sources 398 (2018) 201–208.
[23] S.F. Ho, A. Mendoza-Garcia, S. Guo, K. He, D. Su, S. Liu, O. Metin, S. Sun, A facile route to monodisperse MPd (M = Co or Cu) alloy nanoparticles and their catalysis for electrooxidation of formic acid, Nanoscale 6 (2014) 6970–6973.
[24] N. Yang, Z. Zhang, B. Chen, Y. Huang, J. Chen, Z. Lai, Y. Chen, M. Sindoro, A.L. Wang, H. Cheng, Z. Fan, X. Liu, B. Li, Y. Zong, L. Gu, H. Zhang, Synthesis of ultrathin PdCu alloy nanosheets used as a highly efficient electrocatalyst for formic acid oxidation, Adv. Mater. 29 (2017).
[25] M. Luo, S. Guo, Strain-controlled electrocatalysis on multimetallic nanomaterials, Nat. Rev. Mater. 2 (2017) 17059.
[26] J. Wu, P. Li, Y.T. Pan, S. Warren, X. Yin, H. Yang, Surface lattice-engineered bimetallic nanoparticles and their catalytic properties, Chem. Soc. Rev. 41 (2012) 8066–8074.
[27] M. Ren, Y. Zhou, F. Tao, Z. Zou, D.L. Akins, H. Yang, Controllable modification of the electronic structure of carbon-supported core-shell Cu@Pd catalysts for formic acid oxidation, J. Phys. Chem. C 118 (2014) 12669–12675.

[28] M. Lopez-Haro, K. Yoshida, E. Del Rio, J.A. Perez-Omil, E.D. Boyes, S. Trasobares, J.M. Zuo, P.L. Gai, J.J. Calvino, Strain field in ultrasmall gold nanoparticles supported on cerium-based mixed oxides. Key influence of the support redox state, Langmuir 32 (2016) 4313–4322.
[29] T. Kawasaki, Y. Takai, R. Shimizu, Distorted surface and interface structures of catalytic gold nanoparticles observed by spherical aberration-free phase electron microscopy, Appl. Phys. Lett. 79 (2001) 3509–3511.
[30] Z. Xi, J. Li, D. Su, M. Muzzio, C. Yu, Q. Li, S. Sun, Stabilizing CuPd nanoparticles via CuPd coupling to WO2.72 nanorods in electrochemical oxidation of formic acid, J. Am. Chem. Soc. 139 (2017) 15191–15196.
[31] X.M. Qu, L.X. You, X.C. Tian, B.W. Zhang, G.D. Mahadevan, Y.X. Jiang, S.G. Sun, CeO2 nanorods with high energy surfaces as electrocatalytical supports for methanol electrooxidation, Electrochim. Acta 182 (2015) 1078–1084.
[32] R.S. Peng, S.J. Li, X.B. Sun, Q.M. Ren, L.M. Chen, M.L. Fu, J.L. Wu, D.Q. Ye, Size effect of Pt nanoparticles on the catalytic oxidation of toluene over Pt/CeO2 catalysts, Appl. Catal. B – Environ. 220 (2018) 462–470.
[33] V. Mazumder, S. Sun, Oleylamine-mediated synthesis of Pd nanoparticles for catalytic formic acid oxidation, J. Am. Chem. Soc. 131 (2009) 4588–4589.
[34] D. Chen, P. Sun, H. Liu, J. Yang, Bimetallic Cu–Pd alloy multipods and their highly electrocatalytic performance for formic acid oxidation and oxygen reduction, J. Mater. Chem. A 5 (2017) 4421–4429.
[35] K. Jiang, P. Wang, S. Guo, X. Zhang, X. Shen, G. Lu, D. Su, X. Huang, Ordered PdCu-based nanoparticles as bifunctional oxygen-reduction and ethanol-oxidation electrocatalysts, Angew. Chem. Int. Ed. 55 (2016) 9030–9035.
[36] K. Miao, Y. Luo, J. Zou, J. Yang, F. Zhang, L. Huang, J. Huang, X. Kang, S. Chen, PdRu alloy nanoparticles of solid solution in atomic scale: outperformance towards formic acid electro-oxidation in acidic medium, Electrochim. Acta 251 (2017) 588–594.
[37] M. Wojdyr, Fityk: a general-purpose peak fitting program, J. Appl. Crystallogr. 43 (2010) 1126–1128.
[38] Y. Luo, L. Calvillo, C. Daiguebonne, M.K. Daletou, G. Granozzi, N. Alonso-Vante, A highly efficient and stable oxygen reduction reaction on Pt/CeOx/C electrocatalyst obtained via a sacrificial precursor based on a metal-organic framework, Appl. Catal. B 189 (2016) 39–50.
[39] P. Strasser, S. Koh, T. Anniyev, J. Greeley, K. More, C. Yu, Z. Liu, S. Kaya, D. Nordlund, H. Ogasawara, M.F. Toney, A. Nilsson, Lattice-strain control of the activity in dealloyed core-shell fuel cell catalysts, Nat. Chem. 2 (2010) 454–460.
[40] T.H. de Keijser, J.I. Langford, E.J. Mittemeijer, A.B.P. Vogels, Use of the Voigt function in a single-line method for the analysis of X-ray diffraction line broadening, J. Appl. Crystallogr. 15 (1982) 308–314.
[41] R. Si, M. Flytzani-Stephanopoulos, Shape and crystal-plane effects of nanoscale ceria on the activity of Au-CeO2 catalysts for the water-gas shift reaction, Angew. Chem. Int. Ed. Engl. 47 (2008) 2884–2887.
[42] M. Mavrikakis, B. Hammer, J.K. Nørskov, Effect of strain on the reactivity of metal surfaces, Phys. Rev. Lett. 81 (1998) 2819–2822.
[43] Y. Lu, Y. Jiang, X. Gao, X. Wang, W. Chen, Strongly coupled Pd nanotetrahedron/tungsten oxide nanosheet hybrids with enhanced catalytic activity and stability as oxygen reduction electrocatalysts, J. Am. Chem. Soc. 136 (2014) 11687–11697.
[44] H.A. Miller, A. Lavacchi, F. Vizza, M. Marelli, F. Di Benedetto, F. D'Acapito, Y. Paska, M. Page, D.R. Dekel, A Pd/C-CeO2 anode catalyst for high-performance platinum-free anion exchange membrane fuel cells, Angew. Chem. Int. Ed. 55 (2016) 6004–6007.
[45] Q. Lv, Q. Meng, W. Liu, N. Sun, K. Jiang, L. Ma, Z. Peng, W. Cai, C. Liu, J. Ge, L. Liu, W. Xing, Pd–PdO interface as active site for HCOOH selective dehydrogenation at ambient condition, J. Phys. Chem. C 122 (2018) 2081–2088.
[46] L.A. Kibler, A.M. El-Aziz, R. Hoyer, D.M. Kolb, Tuning reaction rates by lateral strain in a palladium monolayer, Angew. Chem. Int. Ed. Engl. 44 (2005) 2080–2084.
[47] S. Hu, L. Scudiero, S. Ha, Electronic effect on oxidation of formic acid on supported Pd–Cu bimetallic surface, Electrochim. Acta 83 (2012) 354–358.
[48] T. Bligaard, J.K. Nørskov, Ligand effects in heterogeneous catalysis and electrochemistry, Electrochim. Acta 52 (2007) 5512–5516.
[49] M. Wakisaka, S. Mitsui, Y. Hirose, K. Kawashima, H. Uchida, M. Watanabe, Electronic structures of Pt−Co and Pt−Ru alloys for CO-tolerant anode catalysts in polymer electrolyte fuel cells studied by EC−XPS, J. Phys. Chem. B 110 (2006) 23489–23496.
[50] X. Zhao, J. Zhu, L. Liang, C. Liu, J. Liao, W. Xing, Enhanced electroactivity of Pd nanocrystals supported on H3PMo12O40/carbon for formic acid electrooxidation, J. Power Sources 210 (2012) 392–396.
[51] J.X. Liu, Y.Q. Su, I.A.W. Filot, E.J.M. Hensen, A linear scaling relation for CO oxidation on CeO2-supported Pd, J. Am. Chem. Soc. 140 (2018) 4580–4587.
[52] R.R. Adžić, A.V. Tripković, W.E. O'Grady, Structural effects in electrocatalysis, Nature 296 (1982) 137.
[53] H. Duncan, A. Lasia, Separation of hydrogen adsorption and absorption on Pd thin films, Electrochim. Acta 53 (2008) 6845–6850.
[54] F.L. Wang, H.G. Yu, Z.Q. Tian, H.G. Xue, L.G. Feng, Active sites contribution from nanostructured interface of palladium and cerium oxide with enhanced catalytic performance for alcohols oxidation in alkaline solution, J. Energy Chem. 27 (2018) 395–403.
[55] W.H. Yang, Q.H. Zhang, H.H. Wang, Z.Y. Zhou, S.G. Sun, Preparation and utilization of a sub-5 nm PbO2 colloid as an excellent co-catalyst for Pt-based catalysts toward ethanol electro-oxidation, New J. Chem. 41 (2017) 12123–12130.
[56] L.G. Feng, J.F. Chang, K. Jiang, H.G. Xue, C.P. Liu, W.B. Cai, W. Xing, J.J. Zhang, Nanostructured palladium catalyst poisoning depressed by cobalt phosphide in the electro-oxidation of formic acid for fuel cells, Nano Energy 30 (2016) 355–361.